Quantitative biometry of zebrafish retinal vasculature
using optical coherence tomographic angiography

by

Ivan Bozic

Thesis

Submitted to the Faculty of the

Graduate School of Vanderbilt University

in partial fulfillment of the requirements

for the degree, of

MASTER OF SCIENCE

in

Biomedical Engineering

May 11, 2018

Nashville, Tennessee

Approved:

Yuankai K. Tao, PhD

Justin Baba, Ph.D.

TABLE OF CONTENTS

LIST OF FIGURES

INTRODUCTION

As of 2010, there were an estimated 285 million visually impaired and 39 million blind individuals worldwide [1]. In the United States, proliferative diabetic retinopathy (PDR) and wet age-related macular degeneration (AMD) are two of the leading causes of severe vision-loss and blindness [1, 2]. PDR is a complication of diabetes that is characterized by neovascularization originating from the retina and optic disc, that can result in hemorrhage, fibrosis, traction, and retinal detachment [3, 4]. An estimated 415 million adults suffer from diabetes globally, and almost half of all diabetics are expected to experience some degree of retinopathy [4, 5]. AMD is the leading cause of blindness among people aged 55 and older in the developed world and affect more than 1.75 million individuals in the United States [6, 7]. Wet AMD is characterized by neovascularization, that often leads to hemorrhage and exudation. While only 10 percent of AMD patients develop wet AMD, severe vision-loss progresses quickly in the majority of these patients [6].

Vascular endothelial growth factor (VEGF) inhibitors have become standard treatments for both PDR and wet AMD [8, 9]. Intravitreal anti-VEGF injection has been shown to significantly stabilize visual acuity (VA), with 91.5-95.4% of wet AMD patients in one clinical study showing less than a 15-letter decrease in VA [10]. However, anti-VEGF treatment has been suggested to be less effective at maintaining VA, and one study showed that 34% of patients experienced a VA loss of >15 letters after five years of treatment [11]. One major limitation of anti-VEGF therapy is the need for repeated injections on either a monthly or as-needed basis (~6-7 injections per year) [4] [10, 13]. In addition to patient anxiety, repeat injections also increase the risk of side effects such as endophthalmitis [15]; acute increases in intraocular pressure requiring topical or surgical anti-glaucoma interventions [16]; and off-target drug effects including loss of retinal ganglion cells and circulation disturbances in the choriocapillaris [9]. The aforementioned limitations of the current clinical standard-of-care and a lack of understanding of the structural, metabolic, and vascular changes underlying retinal neovascularization highlights the need to identify mechanisms of pathogenesis and novel anti-angiogenic therapies.

The zebrafish (*Danio rerio*) is a popular model organism because its fecundity and life cycle have enabled development of mutant phenotypes of human pathologies and they are well-suited for large scale experiments [17, 18]. As an ophthalmological model, the zebrafish retina shares similar structure and function with that of humans and other vertebrates [22]. Similar to humans, the zebrafish retina is composed of seven major cell types (six neural and Müller glial cells), three nuclear layers separated by two plexiform layers, and a highly ordered mosaic organization of neurons in each layer [23, 24]. As diurnal species, humans and zebrafish have cone-dominant vision, in contrast to the rod-dominant vision found in mice; this has advantages for studying cone degeneration diseases such as AMD [24, 25].

Zebrafish readily absorb compounds from their aqueous environment and are also affected byt them, which allows for induction of pathologies and delivery of chemical compounds without the need for injections [21]. Retinal vasculopathies can be modeled by exposing animals to hypoxic water for 3-10 days to induce neovascularization and vascular leakage. Similarly, exposure to glucose induces hyperglycemia, which has been shown to result in retinal structural abnormalities similar to those in DR [25]. As a pharmacological model, 82% of disease-causing human proteins

have orthologues in zebrafish, and pharmacological effects are highly conserved between human and zebrafish [26][27][28].

The majority of drug screens in zebrafish are performed using larval animals because their transparency and size are well-suited for imaging and housing in large-scale studies [29]. However, normal vascular development [30] and differences in inflammatory and immune responses between larva and adults [30] may confound structural and functional changes in larval zebrafish models of DR. In this study, we demonstrate *in vivo* retinal imaging in adult zebrafish (≥3 months post-fertilization, mpf) using optical coherence tomography (OCT) [31] and OCT angiography (OCT-A) [32] and present post-processing algorithms for vascular segmentation and biometry. Quantitative measurements of retinal perfusion and angiogenesis during longitudinal studies can provide insights into disease pathogenesis and therapeutic efficacy in drug screens for novel anti-angiogenic compounds. In addition to tracking functional changes, retinal vascular biometry can also be used as a method for uniquely identifying individual animals with high sensitivity and specificity. To this end, we developed and validated a novel identification method that obviates the need for physical marking methods such as elastomer marking, freeze branding, removal of specific scales, fin clipping, and dorsal fin tagging [33]. We believe the retinal vascular biometry methods presented here are robust enabling technology that will broadly benefit large-scale zebrafish studies.

Imaging system

OCT and OCT-A imaging of wild-type zebrafish was performed using a custom-built spectral domain OCT (SD-OCT) system (Fig. 1(a)). A superluminescent diode (InPhenix) with 855 nm central wavelength and 90 nm bandwidth was split between reference and sample arms using an 80:20 coupler, respectively. The intensity was detected using the central 2048 pixels of a 4096 pixels linear CMOS array with 125 kHz line-rate (spL4096-140km, Basler). Measured system SNR was 107 dB with -6 dB falloff at 1.1 mm and 2.56 µm axial resolution in tissue. Zebrafish were imaged using a 1 mm diameter spot size at the pupil with 700 µW of optical power.
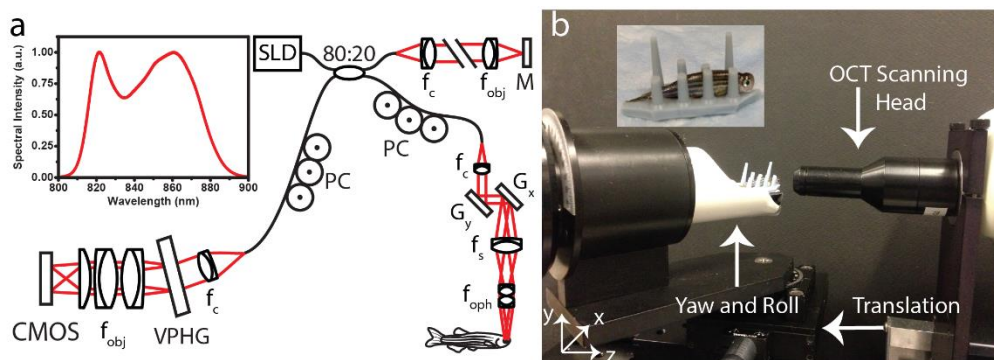

Fig. 1. Imaging system. (a) Custom-built SD-OCT system. CMOS, detector; f, collimating, objective, ophthalmic, and scan lenses; G, galvanometers; M, mirror; PC, polarization controller; SLD, superluminescent diode; VPHG, grating. Zebrafish retina were imaged in air through a contact lens and positioned using a custom holder (inset). (b) 5-axis alignment stage.

Imaging protocol

In vivo imaging was performed under an animal protocol approved by the Institutional Animal Care and Use Committee (IACUC) at Cleveland Clinic. Ten adult wild-type zebrafish (≥3 mpf) were imaged repeatedly during two sessions on ten different days over four weeks. Both eyes were imaged during each imaging session (20 total datasets per eye). Repeat imaging sessions on each day were separated by a two-hour break and imaging days were separated by 48 hours.

Animals were anesthetized prior to imaging using a 0.14% Tricaine solution. Anesthetized animals were positioned using a custom holder and the retina was imaged through a contact lens (Fig. 1(b)) [41] . Zebrafish OCT and OCT-A volumetric datasets were centered on the optical nerve head (ONH) using a 5-axis stage (Fig. 1(b), Leica Microsystems). OCT volumes consisted of 2500 B-scans (2048 x 500 pix.) acquired in approximately 10 s. These datasets included five repeated B-scans at each lateral position for OCT-A post-processing. Animal imaging and handling were performed in less than 10 minutes followed by recovery, during which water was forced across the gills to maximize animal survival for the duration of the study [41]. Between

imaging days, fish were housed in light exposure and temperature controlled rooms in separate boxes and grouped so that individual animals were uniquely identifiable by their strip/spots patterns and caudal fin cuts.

Vessel segmentation and labeling

Vessel segmentation, labeling, and feature extraction were performed on *en face* OCT-A projections using custom developed algorithms (Fig. 2). The steps are grouped into four categories to better represent the processing pipeline. Each step is described in detail in the following sections.
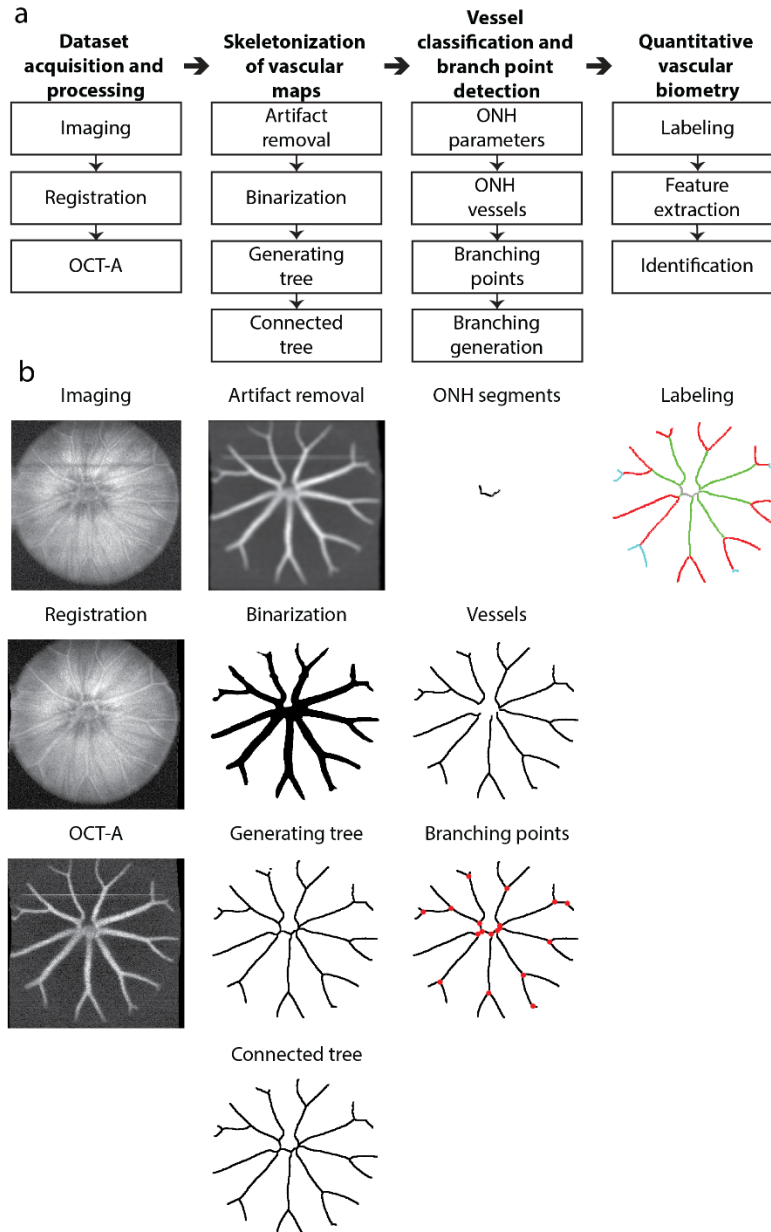

Fig. 2. Processing algorithm. (a) Algorithm block diagram showing a flow chart of vessel segmentation, labeling, and feature extraction; and (b) Processing results in each step.

Dataset acquisition and processing

Raw OCT B-scan bulk motions were removed using discrete Fourier transform cross-correlation [42]. First, repeated B-scans at the same location were registered to each other. The resulting registered B-scans were then averaged, and all of the averaged B-scans in the volumetric dataset was registered. Volume registration parameters were calculated using OCT data and applied to the corresponding OCT-A frames.

OCT-A vasculature maps were calculated using weighted optical microangiography (wOMAG) [43]. wOMAG uses OCT intensities to remove OCT-A artifacts caused by tissue hyper-reflectivity. Here, raw optical microangiography (OMAG) frames were weighted by an intensity decorrelation function, $(D/D_0)^n$. The decorrelation coefficient, D, represents the intensity decorrelation between repeated B-scans, and optimal values for D_0 and n were experimentally determined ($D_0 = 0.1$, n = 0.5).

Skeletonization of vascular maps

En face OCT-A projections were lowpass filtered to smooth vessel contours and remove speckle noise. A vertical intensity gradient was also calculated and subtracted from the filtered vessel maps to remove breathing artifacts (horizontal streaks). The resulting OCT projections were then binarized and skeletonized using dilatation and erosion [44]. Morphological dilatation and erosion were performed to expand and compress the binary images. Dilated OCT-A projection was performed using a circular kernel (5 pixels radius) for unification of the vessel thickness. This was followed by erosion to obtain a one pixel width skeleton.

Vessel classification and branch point detection

Skeletonized vasculature maps were used to detect vessel branch points. Vessels were first classified as either ONH or retinal vessels. The retinal pigment epithelium (RPE) was segmented from OCT cross-sections [45] and the ONH was identified by the discontinuity in the RPE. The resulting ONH segmentation was then fit to a circle defined by the ONH center and radius. All vessel branches within the ONH radius were classified as ONH vessels and all remaining vessels were further processed for branch point identification.

A set of 18 predefined 3x3 pixel branch kernels was created to represent all possible orientations of vessel bifurcation and trifurcation (Fig 3). The spatial location of each vessel branch point was identified by convolving the skeletonized vasculature map with each kernel. Branch points were then used to classify each vessel segment by branch generation relative to the ONH (Fig. 4).
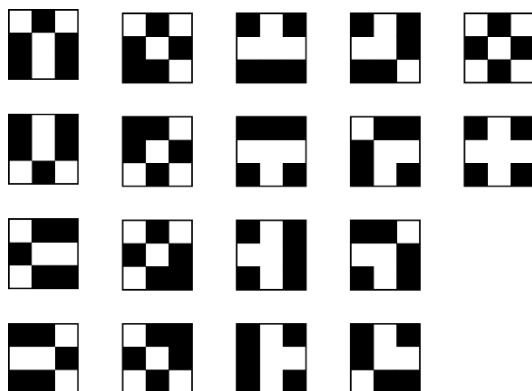

Fig. 3. Branch kernel matrix. 18 predefined 3x3 pixel kernels were created to represent all possible vessel branch orientations.

<u>Quantitative vascular biometry</u>

Quantitative biometry was performed by extracting vessel segment length, curvature, and branch angle between branch points in the skeletonized vessel map (Fig. 4). Segment length was defined as the total number of pixels in each vessel segment, curvature was calculated as the ratio between the vessel segment length and Euclidean distance between corresponding branch points, and angle was calculated as the angle between vessel segments. Vascular biometrics were extracted for each vessel branch originating from the ONH beginning at the 12 o'clock position and moving clockwise around the ONH.
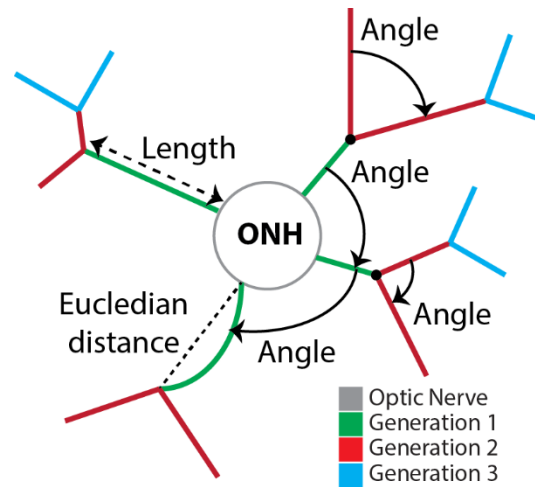

Fig. 4. Quantitative vascular biometry. Angle, curvature, and length were defined on skeletonized vascular maps. All branch generations are referenced with respect to their connectivity relative to the ONH.

Retinal vascular biometry for animal identification

Retinal vascular biometry was evaluated as a robust, noncontact, and noninvasive method for unique zebrafish identification over longitudinal timepoints. A Pearson correlation coefficient matrix was calculated by comparing vessel branch length, curvature, and angle between all datasets. A weight averaged was then used to combine correlation matrices for each generation into a single correlation matrix between all datasets. Here, the weighted average favored contributions from lower generations to compensate for variability in OCT/OCT-A FOV at longitudinal timepoints, which may result in inconsistent biometrics from higher generation vessel branches.

Correlation coefficients in the first-generation matrix above a threshold of 0.957 were exactly reproduced in the overall correlation coefficient matrix for the associated fish. Correlation coefficients below 0.957 in the first generation were combined with correlation coefficients from subsequent generations by a weighted mean method. The optimal threshold of 0.957 was empirically determined by calculating sensitivity and specificity at various thresholds. The highest sensitivity and specificity occurred at a threshold of 0.957 (Fig. 5).

Coefficients were assigned relative weights of 6, 7, and 4 for generations 1, 2, and 3, respectively. A weight of 2 was assigned for coefficients in generations 4 through 6. The optimal weight for each generation was empirically determined by calculating sensitivity and specificity values with various weights of coefficients (1-10, sensitivity and specificity values were found to

increase to a maximum and then decrease within this range). Correlation coefficients for higher generations in fish that did not have branches in these generations were excluded from weighted mean calculations. The ten largest overall correlation coefficients for each fish were selected to identify the images from the respective ten time points.
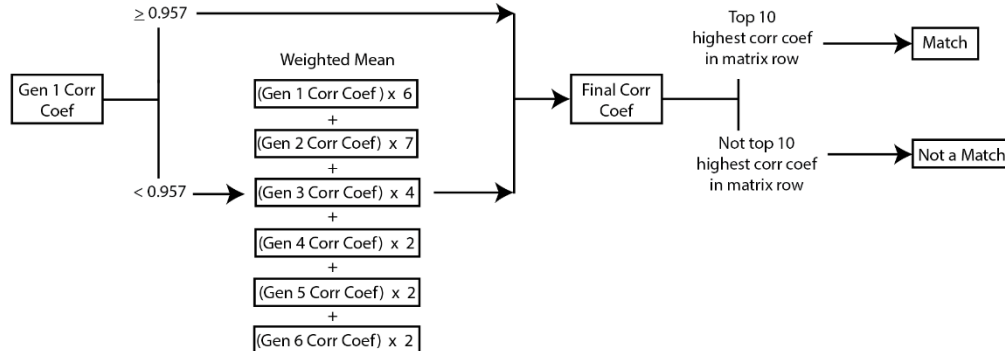

Fig. 5. Identification schematic. Every correlation coefficient (Corr Coef) in the first generation (Gen 1) matrix was processed in this manner to produce the final correlation coefficient in the overall coefficient matrix. After construction of the overall coefficient matrix was completed, fish were matched by selecting the highest ten (corresponding to the ten time points) correlation coefficients of each row.

In vivo OCT and OCT-A volumes, sampled with 2048 x 500 x 2500 pix. (spectrum x A-scan x 5-repeated B-scans), were acquired in approximately 10 s. A representative OCT dataset centered on the ONH is presented in Figure 6 with cross-sectional retinal layers labeled based on previous studies comparing OCT cross-sections to corresponding histology (Fig. 6(b)) [46, 47]
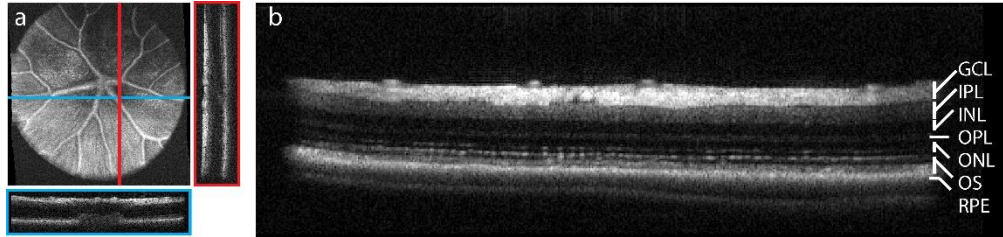

Fig. 6. *In vivo* retinal OCT in zebrafish. (a) *En face* OCT projection with representative orthogonal cross-sections (blue/red lines and insets). (b) 5-frame averaged OCT cross-section with labeled retinal layers. GCL, ganglion cell layer; IPL, inner plexiform layer; INL, inner nuclear layer; OPL, outer plexiform layer; ONL, outer nuclear layer; OS, outer segment; and RPE, retinal pigment epithelium.

The corresponding *en face* OCT-A projection shows central major vessels radiating outward from the ONH (Fig. 7). OCT-A B-scans show vessel cross-sections at the surface of the retina and flow artifacts at the RPE below each vessel. We distinguish retinal vessels from artifacts by segmenting and isolating only the upper layer of flow signals (Fig. 7(a), arrows) because in the adult zebrafish, the retinal vasculature forms a membranous layer that is attached to the vitreal interface [48].
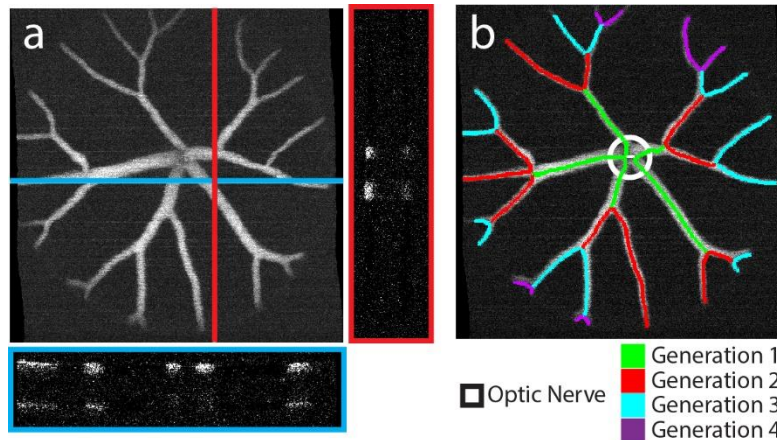

Fig. 7. *In vivo* retinal OCT-A in zebrafish. (a) *En face* OCT-A projection with representative orthogonal cross-sections (blue/red lines and insets) showing retinal vessels (arrow) and RPE artifacts. (b) OCT-A projection with corresponding segmentation mask overlay. Vessel branches are color-coded based on their branch generation relative to the ONH (white circle).

OCT-A vessel maps were skeletonized and the resulting vessel segments were color-coded to represent different branches relative to the ONH (Fig. 7(b)). Any skeletonized vessel segments that begin and end within the ONH (white circle) were ignored. Vessels that begin inside and end outside of the ONH were considered the first branch generation (green) and branch generations were incremented radially outward from the ONH. Total processing time for each OCT-A dataset was approximately 13 minutes, the bulk of which was spent on volumetric registration (>12 min.). Skeletonization and vessel segmentation was performed in ~30 s per vascular map.

Automatically segmented vessel maps were evaluated by manual graders to quantify the robustness of our algorithm. Errors were identified in 2.5% of data (5 of 200 vessel maps) and classified as either segmentations errors at the periphery of the FOV (Fig. 8) or inside the ONH (Fig. 9). Figures 8 and 9 show longitudinal datasets in the same eye to highlight these segmentation errors. At the edge of the FOV, segmentation is confounded by areas of low OCT-A contrast and cropped vessel branches. Poor contrast results in missed branches and branch points (Fig. 8, pink arrows). Similarly, vessels cropped at the end of the imaging FOV may result in missed branch points (Fig. 8, orange arrows). Missing branches or branch points confound all downstream analyses, including branch generation labeling and quantification of branch length, angle, and curvature. Mislabeled branch generations also occurred because of overlap between a vessel branch point and the ONH rim. In these cases, there was ambiguity in classifying the vessel segment as either a retinal or ONH vessel, which led to the mislabeling of subsequent branch generations originating from the initial mislabeled ONH branch (Fig. 9).
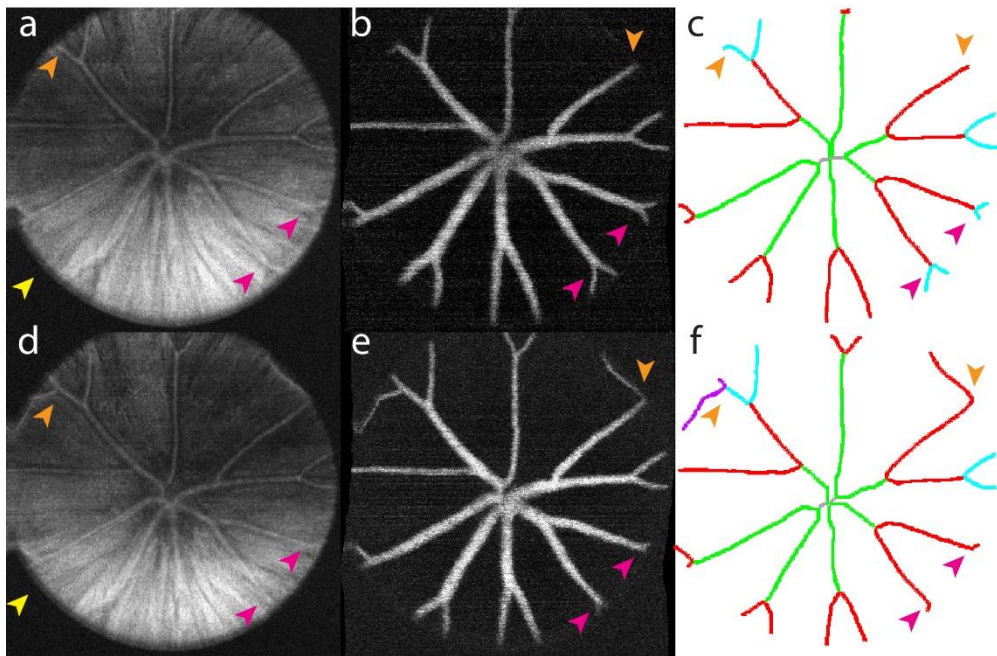
Fig. 8. Segmentation errors at the FOV periphery. Representative *en face* (a), (d) OCT, (b), (e) OCT-A, and (c), (f) segmentation maps at two longitudinal timepoints. Generation 3 branches, which are identified are misidentified as part of the preceding generation 2 branch because of poor contrast (pink arrows). Similarly, vessel branches cropped by the edge of the FOV with sufficient contrast may be misidentified as part of the preceding generation (orange arrows).

Automatically extracted quantitative vascular biometrics were color-coded and plotted as maps of vessel branch angle, curvature, and length to enable qualitative comparisons between longitudinal data and eyes (Fig. 10). Biometrics were grouped by left (OS) and right (OD) eye in each fish, and all 10 repeated longitudinal datasets in each eye were shown as vertical columns. In the horizontal axis, branch segments (row) were grouped by branch generations. Visibly, the biometric data becomes noisier in higher generation vessel branches because of aforementioned segmentation errors at the edge of the FOV. Within each eye, similar biometric patterns are observed in repeated datasets for each eye, but data between different eyes and different fish are significantly different.
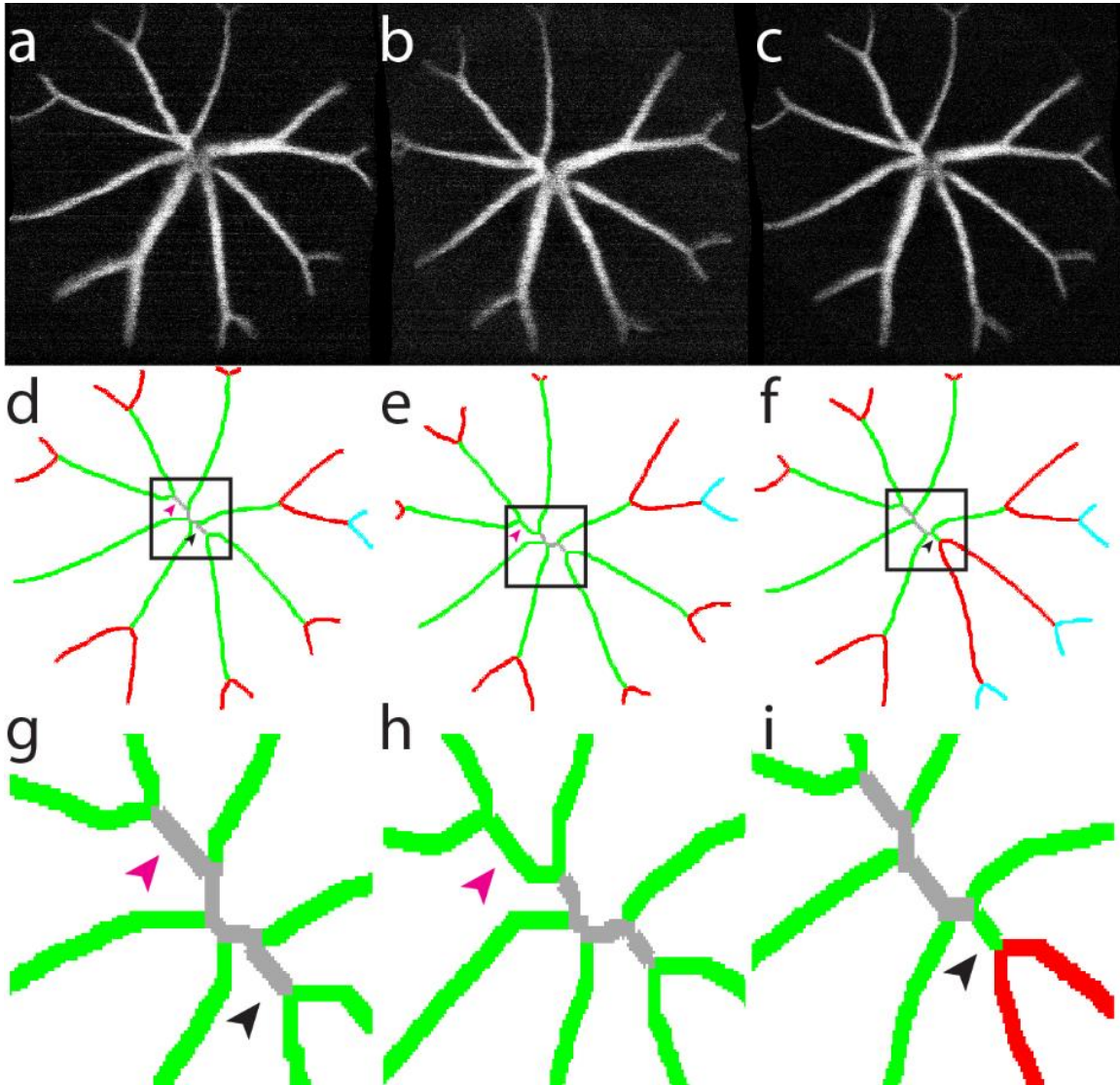

Fig. 9. Segmentation errors at the ONH. (a)-(c) *En face* OCT-A, (d)-(f) segmentation maps, and (g)-(i) magnified views around the ONH at three longitudinal timepoints. (d), (g) Correctly labeled datasets show ONH vessels in gray. (e), (g), (f), (i) Branch generation labeling errors show ONH vessels labeled as first-generation vessels (green).
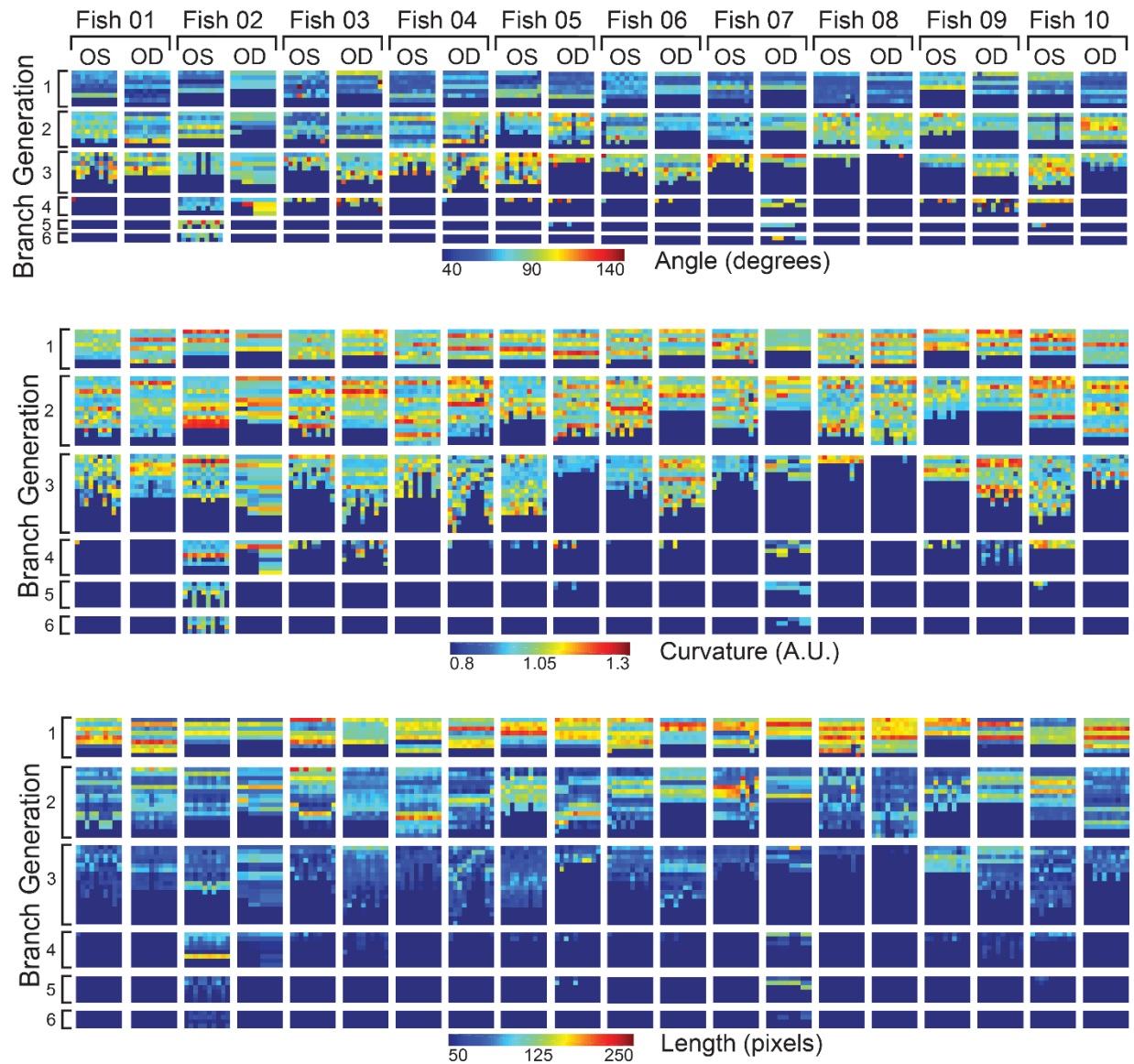
10

Fig. 10. Quantitative vascular biometry. Vessel branch (a) angle, (b) curvature, and (c) length of 10 repeated longitudinal datasets (columns) for both eyes of 10 zebrafish (column groups). Biometrics in each eye were grouped by branch generation (row groups) and each row shows biometric data from each vessel in the respective generation.

Branch vessel length was identified as the most robust biometric parameter for comparing vascular data between longitudinal timepoints because it has the highest dynamic range and lowest noise of all three parameters (Fig 10.). When comparing branch vessel lengths, higher order generations (>3) were given lower weights because of increased noise as compared to the first two generations (Fig. 11). The increased noise is attributed to differences in imaging FOV between longitudinal timepoints that result in different higher generation branch vessels being visible (Fig. 11(b)-(d)).
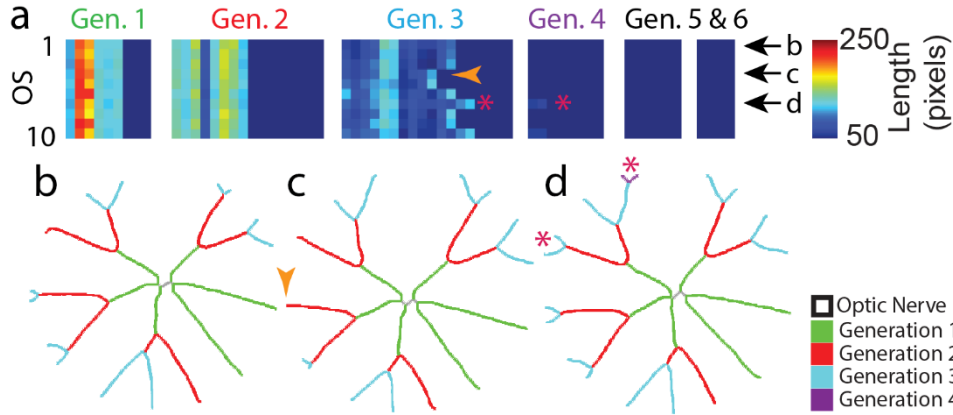
Fig. 11. Vessel branch length comparison between longitudinal timepoints. (a) Representative biometric map showing vessel branch length differences between 10 repeated datasets in one eye. (b)-(d) Segmented vascular maps at 3 timepoints showing similar length parameters in the first and second vessel generations and increased noise in higher generations as a result of FOV differences (asterisk).

As explained in the methods, the identification process uses only first generation cross-correlation coefficients higher or equal to 0.957. This assumption is reasonable because the first generation is more robust to the changes in images between imaging time points. FOV changes influence first generation feature parameters slightly because they start inside the ONH and in most cases they have branching inside the field of view. Although not all first-generation vessels branch inside the FOV, errors in these cases are relatively small with respect to vessel length and do not influence angle measurements at all. Curvature is influenced by such errors only if the missing part of the vessel has a strong curve in that area. On the other hand, the dynamic range of feature values (especially for length) is much higher than in other generations (Fig 10.). This allows us to consider the first-generation as more robust compared to the others. Figure 12 illustrates changes between two eyes in the first generation.

As described above we decided to weight higher the first branch generation of blood vessel features for automatic identification based on the higher relative change in the features across fish as compared to higher generations. Changes in higher order generations may be influenced by eye position in the field of view (FOV) in images, leading to segmentation errors. Prior to manually fixing these errors, a specificity of 99.82% and a sensitivity of 96.5% was achieved.

After applying the weighted algorithm to the manually corrected dataset, 1986 out of 2000 matches (20 eyes, 10 matches for each eye) were identified correctly (99.3% sensitivity). 37986 out of 38000 matches were correctly identified as mismatches (99.96% specificity). Overall, 18 out of 20 eyes matched all ten timepoints correctly. The remaining two eyes had images from two timepoints each that did not match completely with all of the other timepoints of the associated fish (14 images in total that did not match correctly).
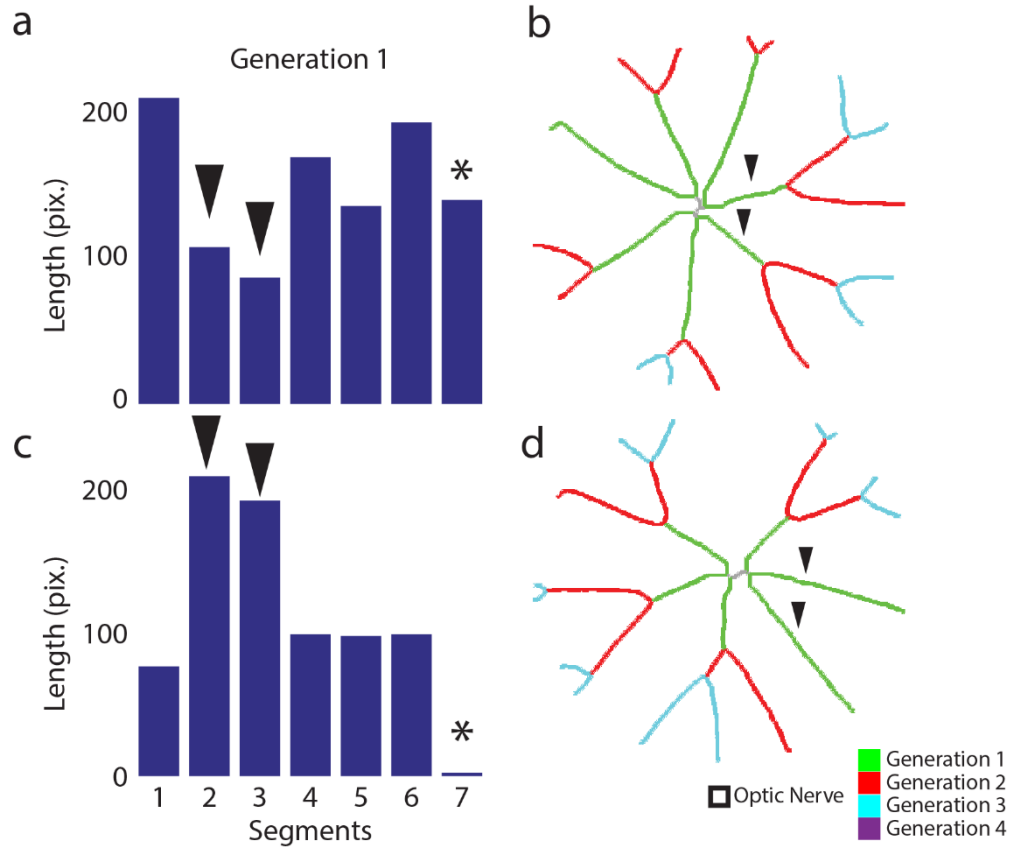
12

Fig. 12. First generation length differences between eyes. (a) and (c) represent length of each segment in the first generation of the two eyes. (b) and (d) shows vasculature maps of those two eyes. Black arrows point out differences between segments on the eyes. Black asterisk denote segment that appear on one eye but not on the other.

DISCUSION AND CONCLUSION

A novel zebrafish identification method has been presented that is efficient and robust. Total processing time for vascular segmentation and labeling was ~30 s, and the identification algorithm showed a sensitivity and specificity above 99%. The algorithm correctly identified 18 out of 20 eyes in each imaging session. The proposed method addresses major limitations in large population imaging studies of adult zebrafish, specifically the need to uniquely identify animals between longitudinal timepoints. The ability to uniquely identify eyes with high specificity and sensitivity reduces the need for fin cutting and housing animals in limited groups (4-5 fish) to enable identification based on natural markings. OCT-A is demonstrated to provide functional information to enable quantitative biometrics in zebrafish models of retinal vascular pathologies.

In the preliminary study, identification errors were primarily a result of differences in FOV between longitudinal timepoints. Translational differences in FOV between timepoints affects the vessel branches that are visible, which contributes to increased noise in biometric parameters for higher order generations. Rotational differences of the FOV at different timepoints also limits the accuracy of biometric comparisons because branch vessels may be mislabeled between datasets. Both sources of error may be addressed using volumetric registration of images at different timepoints at the expense of computational complexity and time. FOV differences also introduced segmentation errors. Vessel branches that are cropped at the edge of the FOV may cause branch points to be missed during automatic feature identification. The current algorithm defines branch points as the point where a parent branch ramifies into two or three children branches. Loss of children branches by FOV cropping can result in parent and a child branch to be considered as a single vessel branch, thus resulting in significant errors in biometric quantification (Fig. 10). A potential solution for overcoming these errors may be to omit any higher generation branch vessels that intersect the FOV edge to avoid the potential for associated errors. ONH segmentation errors were also observed between timepoints. Inaccurate identification of ONH vessels resulted in vessel generation labeling errors for all subsequent branch vessels. One possible solution for ONH vessel segmentation errors may be to appropriately threshold for first generation branches because ONH vessels are significantly shorter than first generation vessels.

The major bottleneck of the current algorithm is volumetric registration, which was ~12 min per volume. However, registration does not significantly limit the utility of the method because it is performed during post-processing and therefore real-time operation is not required. In addition, it was determined that registration of repeated OCT-A frames at the same position was not necessary in all fish. Thus, increased OCT/OCT-A imaging speeds may obviate the need for volumetric registration to remove bulk motion noise.

Demonstration of the use of OCT and OCT-A for structural and functional imaging of zebrafish retina has been accomplished. Quantitative vascular biometry was extracted from automatically segmented vessels from OCT-A and used to uniquely identify eyes in different fish between longitudinal timepoints. Identification accuracy of 99.3% was achieved in a preliminary study of wild-type fish over 10 repeated timepoints. The developed technology eliminates the need to manually mark and identify animals and provides quantitative metrics for studying functional changes in zebrafish models of retinal pathologies.

REFERENCES

1.   Tadayoni, R., et al., *A Randomized Controlled Trial of Alleviated Positioning after Small Macular Hole Surgery.* Ophthalmology, 2011. **118**(1): p. 150-155.
2.   Rein, D.B., et al., *Forecasting age-related macular degeneration through the year 2050: The potential impact of new treatments.* Archives of Ophthalmology, 2009. **127**(4): p. 533-540.
3.   Shah, K.B. and D.P. Han, *Proliferative diabetic retinopathy.* International ophthalmology clinics, 2004. **44**(4): p. 69-84.
4.   Mohamed, Q.A., A. Ross, and C.J. Chu, *Diabetic retinopathy (treatment).* BMJ Clinical Evidence, 2011. **2011**: p. 0702.
5.   Federation, I.D., *IDF Diabetes Atlas.* International Diabetes Federation, 2015. **7**.
6.   Gragoudas, E.S., et al., *Pegaptanib for neovascular age-related macular degeneration.* New England Journal of Medicine, 2004. **351**(27): p. 2805-2816.
7.   The Eye Diseases Prevalence Research, G., *Prevalence of age-related macular degeneration in the united states.* Archives of Ophthalmology, 2004. **122**(4): p. 564-572.
8.   Kovach, J.L., et al., *Anti-VEGF Treatment Strategies for Wet AMD.* Journal of Ophthalmology, 2012. **2012**: p. 786870.
9.   Simó, R. and C. Hernández, *Intravitreous anti-VEGF for diabetic retinopathy: hopes and fears for a new therapeutic strategy.* Diabetologia, 2008. **51**(9): p. 1574.
10.   Group, T.C.R., *Ranibizumab and Bevacizumab for Neovascular Age-Related Macular Degeneration.* New England Journal of Medicine, 2011. **364**(20): p. 1897-1908.
11.   Wecker, T., et al., *Five-year visual acuity outcomes and injection patterns in patients with pro-re-nata treatments for AMD, DME, RVO and myopic CNV.* British Journal of Ophthalmology, 2016.
12.   Rofagha, S., et al., *Seven-Year Outcomes in Ranibizumab-Treated Patients in ANCHOR, MARINA, and HORIZON.* Ophthalmology, 2013. **120**(11): p. 2292-2299.
13.   Heimes, B., et al., *Compliance von Patienten mit altersabhängiger Makuladegeneration unter Anti-VEGF-Therapie.* Der Ophthalmologe, 2016. **113**(11): p. 925-932.
14.   Senra, H., et al., *Psychological impact of anti-VEGF treatments for wet macular degeneration—a review.* Graefe's Archive for Clinical and Experimental Ophthalmology, 2016. **254**(10): p. 1873-1880.
15.   Sachdeva, M.M., et al., *Endophthalmitis following intravitreal injection of anti-VEGF agents: long-term outcomes and the identification of unusual micro-organisms.* Journal of Ophthalmic Inflammation and Infection, 2016. **6**: p. 2.
16.   Ghasemi Falavarjani, K. and Q.D. Nguyen, *Adverse events and complications associated with intravitreal injection of anti-VEGF agents: a review of literature.* Eye, 2013. **27**(7): p. 787-794.
17.   Rubinstein, A.L., *Zebrafish: from disease modeling to drug discovery.* Current Opinion in Drug Discovery and Development, 2003. **6**(2): p. 218-223.
18.   Zon, L.I. and R.T. Peterson, *In vivo drug discovery in the zebrafish.* Nat Rev Drug Discov, 2005. **4**(1): p. 35-44.

19.   Bilotta, J. and S. Saszik, *The zebrafish as a model visual system.* International Journal of Developmental Neuroscience, 2001. **19**(7): p. 621-629.

20.   Veldman, M.B. and S. Lin, *Zebrafish as a Developmental Model Organism for Pediatric Research.* Pediatr Res, 2008. **64**(5): p. 470-476.

21.   Goldsmith, P., *Zebrafish as a pharmacological tool: the how, why and when.* Current Opinion in Pharmacology, 2004. **4**(5): p. 504-512.

22.   Rao, K.D., et al., *Non-invasive ophthalmic imaging of adult zebrafish eye using optical coherence tomography.* CURRENT SCIENCE-BANGALORE-, 2006. **90**(11): p. 1506.

23.   Fadool, J.M. and J.E. Dowling, *Zebrafish: A model system for the study of eye genetics.* Progress in Retinal and Eye Research, 2008. **27**(1): p. 89-110.

24.   Bibliowicz, J., R.K. Tittle, and J.M. Gross, *Toward a Better Understanding of Human Eye Disease.* Progress in Molecular Biology and Translational Science, 2011. **100**: p. 287-330.

25.   Chhetri, J., G. Jacobson, and N. Gueven, *Zebrafish[mdash]on the move towards ophthalmological research.* Eye, 2014. **28**(4): p. 367-380.

26.   Ringholm, A., et al., *One melanocortin 4 and two melanocortin 5 receptors from zebrafish show remarkable conservation in structure and pharmacology.* Journal of Neurochemistry, 2002. **82**(1): p. 6-18.

27.   Cao, Z., et al., *Hypoxia-induced retinopathy model in adult zebrafish.* Nat. Protocols, 2010. **5**(12): p. 1903-1910.

28.   MacRae, C.A. and R.T. Peterson, *Zebrafish as tools for drug discovery.* Nat Rev Drug Discov, 2015. **14**(10): p. 721-731.

29.   Chang, T.-Y., et al., *Fully automated cellular-resolution vertebrate screening platform with parallel animal processing.* Lab on a Chip, 2012. **12**(4): p. 711-716.

30.   Isogai, S., M. Horiguchi, and B.M. Weinstein, *The Vascular Anatomy of the Developing Zebrafish: An Atlas of Embryonic and Early Larval Development.* Developmental Biology, 2001. **230**(2): p. 278-301.

31.   Huang, D., et al., *Optical coherence tomography.* Science, 1991. **254**(5035): p. 1178-1181.

32.   An, L. and R.K. Wang, *In vivo volumetric imaging of vascular perfusion within human retina and choroids with optical micro-angiography.* Optics Express, 2008. **16**(15): p. 11438-11452.

33.   Jennings, B.R.a.M., *Guidance on the housing and care of Zebrafish.* West Sussex: RSPCA Research Animals Department 2010. **12**.

34.   Duval, M.G., et al., *Longitudinal fluorescent observation of retinal degeneration and regeneration in zebrafish using fundus lens imaging.* Molecular Vision, 2013. **19**: p. 1082-1095.

35.   Kashani, A.H., et al., *Optical coherence tomography angiography: A comprehensive review of current methods and clinical applications.* Progress in Retinal and Eye Research, 2017.

36.   Cade, W.T., *Diabetes-Related Microvascular and Macrovascular Diseases in the Physical Therapy Setting.* Physical Therapy, 2008. **88**(11): p. 1322-1335.

37.   Ehrlich, R., et al., *Age-related macular degeneration and the aging eye.* Clinical Interventions in Aging, 2008. **3**(3): p. 473-482.

38.   Cheung, C.Y., et al., *Quantitative and qualitative retinal microvascular characteristics and blood pressure.* Journal of Hypertension, 2011. **29**(7): p. 1380-1391.

39. Witt, N.W., et al., *A novel measure to characterise optimality of diameter relationships at retinal vascular bifurcations.* Artery Research, 2010. **4**(3): p. 75-80.

40. MacGillivray, T.J., et al., *Retinal imaging as a source of biomarkers for diagnosis, characterization and prognosis of chronic illness or long-term conditions.* The British Journal of Radiology, 2014. **87**(1040): p. 20130832.

41. Bell, B.A., et al., *Retinal Vasculature of Adult Zebrafish: In Vivo Imaging Using Confocal Scanning Laser Ophthalmoscopy.* Experimental eye research, 2014. **129**: p. 107-118.

42. Guizar-Sicairos, M., S.T. Thurman, and J.R. Fienup, *Efficient subpixel image registration algorithms.* Optics letters, 2008. **33**(2): p. 156-158.

43. Huang, Y., Q. Zhang, and R.K. Wang, *Efficient method to suppress artifacts caused by tissue hyper-reflections in optical microangiography of retina in vivo.* Biomedical Optics Express, 2015. **6**(4): p. 1195-1208.

44. Chen, S. and R.M. Haralick, *Recursive erosion, dilation, opening, and closing transforms,* IEEE Transactions on Image Processing, 1995. **4**(3): p. 11.

45. Yang, Q., et al., *Automated layer segmentation of macular OCT images using dual-scale gradient information.* Optics Express, 2010. **18**(20): p. 21293-21307.

46. DiCicco, R.M., et al., *Retinal Regeneration Following OCT-Guided Laser Injury in Zebrafish.* Investigative Ophthalmology & Visual Science, 2014. **55**(10): p. 6281-6288.

47. Bailey, T.J., et al., *Spectral-Domain Optical Coherence Tomography as a Noninvasive Method to Assess Damaged and Regenerating Adult Zebrafish Retinas.* Investigative Ophthalmology & Visual Science, 2012. **53**(6): p. 3126-3138.

48. Alvarez, Y., et al., *Genetic determinants of hyaloid and retinal vasculature in zebrafish.* BMC Developmental Biology, 2007. **7**(1): p. 114.